Enhanced antibiotic wastewater degradation by intimately coupled B-Bi_3O_4Cl photocatalysis and biodegradation reactor: Elucidating degradation principle systematically

Yilin Dong [a,b], Dongyu Xu [a,b], Jie Zhang [a,b], Qiuwen Wang [a,b], Shaoxuan Pang [a,b], Guangming Zhang [a,b], Luiza C Campos [c], Longyi Lv [a,b], Xiaoyang Liu [a,b], Wenfang Gao [a,b], Li Sun [a,b], Zhijun Ren [a,b,*], Pengfei Wang [a,b,*]

a School of Energy and Environmental Engineering, Hebei University of Technology, Tianjin 300401, China

b Tianjin Key Laboratory of Clean Energy and Pollutant Control, Tianjin 300401, China

c Department of Civil, Environmental and Geomatic Engineering, University College London, London WC1E 6BT, United Kingdom

*Correspondence to: Z. J. Ren (E-mail: renzhijun2003@126.com) & P. F. Wang (E-mail: pengfeiwang@hebut.edu.cn)

Abstract

Intimately coupled photocatalysis and biodegradation (ICPB) is an emerging technology that has potential applications in the degradation of bio-recalcitrant pollutants. However, the interaction principles between photocatalysts and biofilms in ICPB have not been well developed. This article covers a cooperative degradation scheme coupling photocatalysis and biodegradation for efficient degradation and mineralization of ciprofloxacin (CIP) using ICPB with B-doped Bi_3O_4Cl as the photocatalyst. In consequence, a removal rate of ~95% is reached after 40 d. The biofilms inside the ICPB carriers can mineralize the photocatalytic products, thus improving the removal rate of total organic carbon (TOC) by more than 20%. Interior biofilms are not destroyed by CIP or photocatalysis, and they adapt to ICPB of CIP by enriching in *Pseudoxanthomonas*, *Ferruginibacter*, *Clostridium*, *Stenotrophomonas* and *Comamonas* and reconstructing their microbial communities using energy produced by the light-excited photoelectrons. Furthermore, this research gives new opinion into the degradation principles of the ICPB system.

Keywords: Photocatalysis, Biodegradation, Intimately coupled, Ciprofloxacin (CIP), Photoelectrons transfer

1. Introduction

As a kind of generally used drugs and refractory organic pollutants (ROPs) existing in various aquatic environments, the environmental fate and toxicological characteristics of antibiotics have attracted much attention (Mirzaei et al., 2017; Leong et al., 2016). Ciprofloxacin (CIP) is one of the most frequently used antibiotics

for the treatment of human bacterial infections, and is also an animal-feed additive for accelerating animal growth (Kolpin et al., 2002; Yu et al., 2016). However, CIP molecules are widely gathered in the aquatic environment after animal use, producing grievous injury to human and animal health by triggering bacterial resistance (Qiao et al., 2018). Moreover, CIP as a fluoroquinolone drug containing F atom is permanent and difficult to be degraded by conventional water treatment technologies, which has become a difficult problem.

Photocatalytic oxidation is a promising mean to partly convert the complicated construction of molecules like CIP into biodegradable products (Zhang et al., 2016), but complete mineralization is economically prohibitive and practically difficult, and the rapid chemical reactions without distinction in the process of photocatalytic oxidation generally cause the accumulation of deleterious by-products and excessive residue of oxidation products (Park et al., 2017; Fu et al., 2021; Wang et al., 2015). Although antibiotics are expected to be biodegraded, a severe bottleneck is the slow or non-existent biodegradation of many antibiotics (Kong et al., 2019; Zhang et al., 2018). At present, the indirect coupling of photocatalytic oxidation pretreatment process and biodegradation process is widely used for antibiotic wastewater treatment. In the indirect coupling technology, photocatalytic oxidation technology, as a pretreatment technology, initially destroys the structure of organic pollutants that are difficult to biodegrade, reducing the toxicity to microorganisms in subsequent biological treatment tank. When the wastewater enters the biological treatment tank, further degradation and mineralization of the organic compounds take place. This can

save operating costs on the premise of improving the mineralization of pollutants. However, there are still some problems, and its feasibility in reality is not ideal. First, the indirect coupling technology does not continuously detoxify and requires two reactors, photocatalytic oxidation and biodegradation, which increases its footprint and construction cost. Secondly, the oxidation by photocatalysis is non selective and occurs rapidly, so it is very difficult to control the product in the readily biodegradable stage, which greatly increases the regulation difficulty of the indirect coupling reactor (Marsolek et al., 2008).

Intimately coupled photocatalysis and biodegradation (ICPB) process emerged in recent years reveals enormous potential to enhance the removal and mineralization of recalcitrant pollutants, and can well solve the disadvantages of indirect coupling technology (Marsolek et al., 2008; Zhou et al., 2015). In a typical ICPB system, photocatalysts are loaded on the outside surface of macro-porous carriers and biofilms are accumulated within the inner macropores. With UV or visible light irradiation, photocatalysis first attacks the refractory contaminants to produce biodegradable intermediate products, which are rapidly depleted and mineralized by the interior microorganism (Marsolek et al., 2015; Li et al., 2012a). Because of the protection of the carrier, the biofilms can well protect them from poisons and oxidants. In addition, it has been proved that microorganisms can stimulate growth, maintain cell metabolism, regulate community structure, and conduce to environmental restoration by using light excited electrons through semiconductor photocatalysis. With the repetition of the complex degradation process, the pollutants are effectively removed.

So far, ICPB has been applied to denitrification, dechlorination, and degradation of dyes and antibiotics, exhibiting its applications potential in actual wastewater treatment (Wen et al., 2012; Zhou et al., 2017; Li et al., 2012b; Xiong et al., 2017). ICPB can overcome the incomplete mineralization by single photocatalysis and the limited efficiency on recalcitrant pollutants by single biodegradation. However, the mutual effect of photocatalysis and biodegradation on each other in ICPB have not been thoroughly explored.

Therefore, we coated porous carriers with B/Bi_3O_4Cl and then cultivated formerly acclimated activated sludge to form biofilms in the carriers. An ICPB system was established by irradiating the carriers with visible light. The removal efficiency, the stability of the novel ICPB system, the resulting biotoxicity, and biotransformation in this process were assessed. In the meantime, the degradation pathway of ICPB was deeply studied. The outcomes confirmed that photocatalytic degradation and microbial metabolic degradation occurred synergistically was an effective mean to improve the removal efficiency of the ICPB process.

2. Materials and methods

2.1. Chemicals and reagents

Ciprofloxacin standards were sourced from Merck KGaA. Methanol, and formic acid employed were of high-performance liquid chromatography (HPLC) grade and were bought from Sigma-Aldrich Co. LLC. (USA). The other chemicals and reagents were of analytical grade and obtained from Kemat Chemical Technology Co. LTD. (Tianjin, China).

2.2. Carrier and B-Bi_3O_4Cl (B-BOC) coating procedure

The carrier employed in this study was a commercial polyurethane sponge cube with an average side length of 10.0 mm (Fig. S1, Supplementary Material). The specific surface area of the carrier is 1.9 m^2/g, containing macropores of 300~800 μm, and the porosity is about 98%.

In this research, cheap and efficient ultrathin B-BOC nanosheets were used as photocatalysts. We synthesized B-BOC using a solvothermal way (Dong et al., 2021). The detailed fabrication methods and characterization of B-BOC are illustrated in the Text S1, Fig. S2 and S3. We took the following measure for coating: first, 2.0 g B-BOC were dissolved in 20 mL C_2H_5OH to obtain a homogeneous suspension, and 2 mL HNO_3 was diffused into the solution. Then, the above-mentioned solution was heated to 80 ℃ under ultrasonic vibration for 30 min. Then, the carrier cubes with a volume ratio of 1:1 (V/V) were added to the above dispersed B-BOC solution, and ultrasound was continued for 30 min. Finally, the loaded carriers were dried at 60 ℃, the resulting coated carrier is called sponge@B-BOC, and the weight ratio of B-BOC loaded on carriers to pure carriers is about 2:1.

2.3. Biofilm cultivation

The activated sludge was collected from aerobic sludge of sewage treatment plant, and cultivated in an internal circulation airlift-driven fluidized bed reactor. The synthetic nutrients contained 432 mg/L $C_6H_{12}O_6$, 137 mg/L peptone, 10 mg/L $(NH_4)_2SO_4$, 50 mg/L KH_2PO_4, 50 mg/L $Na_2HPO_4{\cdot}2H_2O$, 50 mg/L $MgSO_4$, 5 mg/L $CaSO_4{\cdot}2H_2O$ and 10 mg/L $FeCl_3$. Subsequently, 30.0 mg/L CIP was added during

microbial acclimation for about 50 days. After the microbes were acclimated and stabilized, the sponge@B-BOC were mixed in the activated sludge reactor for 10 days for microbial colonization and the nutrient solution was refreshed every two days. Finally, the sponge@B-BOC of growing biofilm was obtained, which was denoted as sponge@B-BOC@biofilm.

2.4. Experimental setup and protocols

The ICPB reactor is an internal circulation airlift-driven fluidized bed reactor with a working volume of 800 mL is presented in Fig. S4. Its configuration details are shown in Text S2. Air was provided to the internal circuit of the reactor through a 35 W aeration pump at the bottom of the reactor. An LED panel (42 W) with a wavelength of 420 to 800 nm was adopted as a visible light source.

The original concentration of CIP in the degradation experiments was 30.0 mg/L. The following control systems were also designed for comparison with the ICPB system: photocatalysis (P) system, which was carried out under visible light without carriers; biodegradation (B) system, which was evaluated with sponge@B-BOC@biofilm, but in the dark; visible-light-induced photocatalysis (PC) system, which used sponge@B-BOC; and adsorption (AD) system, which used sponge@B-BOC without light. All the aforesaid schemes were implemented in individual reactors with the identical configuration.

2.5. Analytical methods

The concentration of CIP was measured by high performance liquid chromatography (HPLC) with UV detection at 270 nm, equipped with a 4.6×250 mm, 5 μm Athena HILIC C18 column. Each sample was filtered through a 0.22 μm membrane filter before analysing. The optimized mobile phase consisted of 20% water/formic acid (9/1, V: V) as phase A, and 80% methanol as phase B at a flow rate of 1.0 mL/min. A 20.0 μL sample was injected into the column, and the column temperature was 40 ℃.

The degradation products of CIP were tested by ultra-performance liquid chromatography tandem mass spectrometry (UPLC-MS). Chromatographic separation of the degradation products was carried out on an ACQUITY UPLC bridged ethylene hybrid (BEH) C18 Column (1.7 μm, 100×2.1 mm) with an injection volume of 20.0 μL. The mobile phase composed of 33% methanol and 67% phosphoric acid aqueous solution (0.5%) at a flow rate of 0.25 mL/min.

Characteristics of B-BOC are shown in Text S3. Sample pretreatment methods for microstructure observation of biofilm by scanning electron microscopy (SEM) and biofilm staining process for confocal laser scanning microscopy (CLSM) imaging were provided in Text S4 and Text S5, respectively. The total organic carbon (TOC) was conducted using a TOC analyzer (Shimadzu, Japan). COD analysis was measured using a COD quick detector (LianHua Tech-Co., Ltd., China).

The activity of biofilm on sponge carrier was analyzed by the measurement of Dehydrogenase Activity (DHA). DHA was determined by triphenyltetrazolium

chloride (TTC) colorimetry. Specific measurement steps were provided in Text S6, and the corresponding standard curve was shown in Fig. S5.

2.6. Photo-electrochemical measurements

Photo-electrochemical characterizations were carried out in a standard three-electrode system by an electrochemical station (CHI660D) where blank or modified stainless steel wire (1.0×1.5 cm) as the working electrode, the carbon rod as the counter electrode, and the Hg/Hg_2Cl_2 electrode as the reference electrode. The electrolyte was 0.5 M $NaSO_4$ solution. We obtained transient photocurrents and electrochemical impedance spectroscopy (EIS). Moreover, the light density employed was 80 mW/cm^2.

2.7. Microbial community analysis

Biological samples were gathered to research the bioconversion that operated when ciprofloxacin was removed from the ICPB system. The microbial community structure was performed by polymerase chain reaction amplification followed by high-throughput sequencing technology (Illumina, Hiseq 2500, USA) and then assayed by Sangon Biotech Co., Ltd. (Shanghai, China). DNA extraction was carried out employing the DNA Spin Kit (Omega Biotek, Norcross, GA, USA). 338F (ACTCCTACGGGAGGCAGCAG) and 806R (GGACTACHVGGGTWTCTAAT) primers were selected to amplify the bacterial 16S rRNA V3-V4.

3. Results and discussion

3.1. ICPB fabrication for CIP degradation

The sponge@B-BOC@biofilm was gained by simple impregnation and biofilm

cultivation, that is, a blank polyurethane sponge was immersed in B-BOC alcohol solution. After a simple heat treatment at 80 ℃ in the ultrasonic apparatus, sponge@B-BOC could be obtained. The sponge@B-BOC@biofilm was then successfully combined by biofilm cultivation on sponge@B-BOC for 10 days, as described in Fig. 1a. SEM images show the surface morphology of the sponge carrier before and after B-BOC coating, exhibiting 300-800 μm macropores and large specific surface area (Fig. 1b). In the Fig 1c, the B-BOC catalysts are more uniformly and densely attached to the bone surface of the sponge carrier, its original network skeleton is fully preserved. Moreover, the high-magnification amplified SEM diagram more fully proves that the catalysts are well loaded onto the bone structure of the sponge carrier, and a catalyst film has been formed, distributed on the bone structure inside and outside the carrier; meanwhile a good deal of B-BOC nanosheets are observed on the sponge surface (Fig. S6a-c). Fig. S6d displays TEM image of ultra-thin B-BOC nanosheets with a size of about 200 nm. The ultra-thin B-BOC nanosheets can provide more reactive sites. X-ray diffraction (XRD) pattern is shown in Fig 1d, which also indicates B-BOC was successfully loaded on the sponge. The XRD peaks of the B-BOC nanosheets reveals a pure monoclinic BOC crystal phase (JCPDS No. 86-2221) (Li et al., 2016). In addition, no other impurity phase is observed, indicating that B doping does not change the crystal phase. This result proves that B-BOC nanosheet is successfully prepared. In addition, the loading effect of the catalysts is well, which is conducive to the occurrence of subsequent photocatalytic reactions. Meanwhile, the rough and uneven surface of the catalysts

facilitates the attachment and growth of microbes.

Fig. 1e and f show the exterior and interior of sponge@B-BOC@biofilm. We can see that both the outside and inside of the carrier are covered with a thick biofilm. After using these carriers for separate biodegradation (B) and intimately coupled photocatalysis and biodegradation (ICPB), the biofilms on the carriers have different performance. As can be observed from Fig. S6e and f, in the B process, there is a certain amount of biofilm inside and outside the carrier after 40 days of operation. However, the biomass and biofilm thickness inside the carrier are not as large as the CIP degradation process by ICPB, and the growth of the biofilm is not as good as the direct coupling process. This may be due to the lack of nutrients. In contrast, the carrier in the ICPB is relatively stable. After 10 days of operation, a portion of the catalysts has been exposed outside the carrier (Fig. 1g, h). After 40 days of reaction, the biofilms on the outside surface of the carrier basically fall off, which is due to the double destructive effect of antibiotics and oxidation of free radicals during the photocatalytic process on microbes, resulting in a large area of biofilms on the surface of the carrier falling off, and a large area of B-BOC are exposed (Fig. 1i). Biofilm shedding on the outside surface of the carrier and exposure of the photocatalysts allow more efficient photocatalytic and biodegradation processes. However, there is still a large amount of biofilm attached to the bone structure inside the carrier (Fig. 1j). The difference between the amount of biofilm inside and outside the carrier also reveals the essence of the ICPB process, that is, when the sponge@B-BOC@biofilm comes into contact with the CIP solution, the photocatalyst attached to the surface of the

carrier catalytic CIP undergoes photocatalytic oxidation reaction, which causes the CIP to be oxidized into small molecules with a relatively simple structure and low toxicity, and the internal microorganisms use these small molecules as carbon sources for their own growth and reproduction to effectively degrade and mineralize the organic matter (Zhang et al., 2010). During the ICPB reaction, microbes can be protected inside the carrier and are not be damaged by free radicals. At the same time, the light-excited photoelectrons can be collected by microorganisms to promote their growth and regulate the microbial community to adapt to the unfavorable environment.

3.2. Enhanced CIP and TOC removal by ICPB

The carrier dosage (volume ratio to reactor solution) and light intensity play important roles on CIP degradation in ICPB system, so the effect of the addition amount of sponge@B-BOC@biofilm and light intensity on the degradation performance of CIP was investigated. As the dosage of sponge@B-BOC@biofilm increased, the removal rate of CIP in ICPB reaction becomes higher and higher, as shown in Fig. 2a. However, the total removal capability is equivalent between 30% and 40% dosages, and very high dosages may affect the light transmittance. Further study was then conducted to determine the optimal light intensity. As shown in Fig. 2b, the optimum light intensity is 50 klux, and the corresponding CIP removal rate could be achieved 91.2% within 12 h. However, the reaction rate of ICPB system decreases slightly with the increase of light intensity (60 klux). This can be attributed to the inhibiting action of strong light intensity on biofilm, which affects the removal

efficiency of CIP in the ICPB system. Therefore, considering the cost of catalyst and energy consumption, we chose 30% sponge@B-BOC@biofilm dosage and 50 klux in the subsequent experiments.

The different results of concentration change protocols during short-term tests (12 h) are presented in Fig. 2c. Under the illumination of visible light (P) alone, CIP cannot be effectively removed, indicating that CIP does not have direct photolysis in visible light. For absorptivity (AD), the final degradation rate of the sponge carriers is 40%. In addition, the bio-removal rate is 51.9% after 12 h, even if the microorganisms had been cultivated in 30.0 mg/L CIP for 50 days. Therefore, we speculate that CIP cannot be effectively degraded in the natural environment. The removal rate of CIP by photocatalytic oxidation (PC) is significantly improved, indicating that the prepared B-BOC catalyst has good visible light response ability. After coupling biodegradation, the degradation rate of ICPB to CIP is higher than that of PC, which is related to the biofilm response behavior on the sponge carrier. On the one hand, the shedding of the biofilm on the outer surface of the carrier exposes wide-spread catalysts and enhances the photocatalytic degradation efficiency of CIP, meanwhile, the adaptation of the biofilms inside the carrier to the environment can also promote their utilization of CIP photocatalytic intermediates.

After fitting the degradation curve of CIP in PC and ICPB with quasi first-order kinetics, the change of reaction rate constant (k) can better reflect the removal rate of CIP in PC and ICPB. The first-order kinetic equation is as follows:

$$\ln(C_t/C_0) = kt \quad (1)$$

Where k (h^{-1}) is the CIP degradation rate constant, t (h) is the reaction time, and C_t and C_0 represent the concentration of CIP at t time and starting time, respectively.

Fig. 2d and Table S1 shows the kinetic parameters of CIP degradation in PC and ICPB. The degradation rate constant k of CIP by photocatalytic oxidation alone is 0.103 ± 0.017 h^{-1}, while the degradation rate constant k of CIP in direct coupling reaction is 0.154 ± 0.019 h^{-1}. It can be seen that ICPB has higher CIP degradation efficiency than PC, which may be related to the utilization of intermediate products by biofilm in ICPB. In ICPB, CIP do not be effectively degraded by organisms, so the degradation of CIP is primarily caused by the oxidation of active species produced by photocatalysis, and these active species have no selectivity for substrates during oxidation reaction. Therefore, the utilization of intermediates by biofilms in the carrier can reduce the competition of intermediates for active species, so that more active species participate in the removal of CIP, making the removal rate of CIP by ICPB faster than that of PC.

This finding can be further confirmed by the UV-vis spectrums of CIP solutions in the degradation process. In Fig. S7a, there is only adsorption in AD, and the characteristic adsorption wavelength (278 nm) of CIP in UV-vis spectra at different times has not changed, only the absorbance is gradually decreasing. The UV-Vis spectrums at different times in B reaction have the same change trend as AD, indicating that the biofilm in B does not directly use CIP for metabolism (Fig. S7b). Li Bing et al. discussed the degradation mechanism of various antibiotics in the activated sludge system, they found that the adsorption of activated sludge was the

main reason for the reduction of CIP concentration (Bing et al., 2010). The difference of CIP adsorption between AD and B is mainly caused by the falling off of biofilm on the inner and outer surfaces of the carrier in B reaction. The absorbance of characteristic absorption wavelength of CIP in PC and ICPB decreases gradually (Fig. S7c, d). The decrease of CIP absorbance is higher than that of PC, indicating that the biofilm on the carrier cannot only survive in adverse environment in ICPB, but also maintain metabolic activity and participate in the removal process of CIP.

The changing trend of TOC and COD in CIP solution during the reaction can also prove the use of photocatalytic intermediates by organisms in ICPB. In Fig. 2e, the degradation efficiency of photocatalytic oxidation on CIP is as high as about 80%, but the removal rate of TOC is much lower than that of CIP, which indicates that photocatalysis has a poor effect on CIP mineralization. On the contrary, the participation of organisms makes the degradation rate of TOC by ICPB significantly improved. The direct utilization of intermediate products by biofilm in ICPB is an important reason for the survival of biofilm inside the carrier, and it is also an important advantage of direct coupling compared with indirect coupling. The same conclusion is reached in the COD analysis (Fig. S8).

To test the stability of ICPB system for degrading CIP, the consecutive B, PC and ICPB with a hydrodynamic residence time (HRT) of 12.0 h were measured for 40 days (Fig. 3a, b). Fig. 3c is the photograph of the entire degradation equipment in this test. After the first few cycles of operation, the removal rate of CIP by the B alone increasingly promoted. This may be due to the absorption capacity of the biofilms.

However, the degradation rate decreases significantly after 22 days, owing to the shedding of the biofilms and the desorption of CIP. The PC system shows favourable removal properties for CIP. However, the PC removal rate begins to decline after 18 days, and the final removal rate can only reach 65.1%. This may be because the catalytic activity of the photocatalysts decreases after a long time of irradiation and operation. Differently from B and PC, the biofilms attach to the outside of the carriers are rapidly shedding in the ICPB process for the first 10 days due to the unstable stage of the reaction, resulting in a variable CIP removal efficiency. Apparently, the CIP concentration decreases gradually and the removal efficiency tends to be stable after 10 days, which may be due to the shedding of the biofilm outside the carriers, thus exposing the photocatalysts to form an ideal ICPB system, indicating that the ICPB system can maintain good degradation stability and adapt to adverse environment.

To test transient free radical intermediates in the PC and ICPB system, ESR pattern was carried out. The ·OH signal caught by DMPO is observed both in the PC and ICPB system in Fig. 3d. Notably, the VB potential of the B-BOC nanosheets shows a higher oxidation potential (2.59 eV) (Shi et al., 2018), consequently the OH^- is oxidated by h^+ to form ·OH (Fig. S9). Compared to PC system, the spectrum intensity of ·OH have little change in the ICPB system. In addition, the e^- on the BOC-B surface is captured by O_2 to form $\cdot O_2^-$ (Fig. S9). In Fig. 3e, the ESR signal of DMPO-$\cdot O_2^-$ appears in both PC and ICPB systems, and the ICPB system exhibits much stronger signal. The enhanced $\cdot O_2^-$ spectrum may be caused by the presence of additional photoelectron transfer between B-BOC and biofilm. The ESR results

indicate that ·OH and $\cdot O_2^-$ are the main active species in the ICPB system.

3.3. Photo-electrochemical measurements

The ICPB process cannot merely be divided into B and PC degradation. Full exposure to visible light caused photoelectrons transfer between the two connected sections (Ding et al., 2018). The links between the photocatalyst and microbes contribute to the degradation of CIP. The electron transfer between B-BOC and microbes was studied by photo-electrochemical experiments under visible light illumination. In electrochemical testing, blank and coated stainless steel mesh were used as photoanode, due to the wire composition and mesh structure of the stainless steel mesh resemble the sponge carrier.

A photocurrent is promptly generated after B-BOC is irradiated with visible light (Fig. 4a), indicating that B-BOC acts as photocatalyst and has the fast photoelectron transmission speed. In theory, when the electrode is covered by microorganisms, the resulting photocurrent will be decreased, because light cannot reach the photocatalysts, and microbes are not sensitive to the illumination of light. Nevertheless, when the electrode is covered by microorganisms, the photocurrent does not decrease or even rise slightly, and the additional photocurrent is due to the photoelectrons transfer between B-BOC and biofilms.

In addition, the electron transport between B-BOC and microbes was further elucidated by photoelectrochemical impedance spectroscopy analysis. It is obvious that the size of the semicircle of ICPB system is smaller than the PC system (Fig. 4b). Therefore, the ICPB system is more conducive to electron transport than the

photocatalysts. This means that the ICPB system can produce more electrons for transfer than the PC system, confirming that there are photoelectrons transfer between B-BOC and microbes under the light.

The open-circuit potential decay (OCPD) results of PC and ICPB system can give further substantial evidence for the existence of electron transfer between B-BOC and microbes. The time dependence of OCPD was operated with light on and off. When the light is on, there is a significant response of 0.12 V open-circuit potential (OCP) under single photocatalyst. When biofilm and catalyst are present together, it can be observed that OCP is enhanced by 0.03 V (Fig. 4c). Obviously, under ICPB system, B-BOC@biofilm shows a slower OCPD rate than that under PC system, indicating the delayed reorganization kinetic of electrons. When the open circuit lighting is interrupted, because of the recombination, the extra electrons are removed, and the OCPD rate is directly relevant to the electron lifetime with the following formula (Li et al., 2018):

$$\tau = \frac{-k_B T}{e}\left(\frac{dV_{OC}}{dt}\right)^{-1} \quad (2)$$

Where, k_B is Boltzmann's constant, T is the temperature, and e is the elementary charge.

The photogenerated electrons lifetime (τ) can be computed by OCPD (Fig. 4d). This demonstrates the electron lifetime of B-BOC@biofilm is longer, indicating the reaction in the ICPB system involves more electrons, which certifies the existence of photoelectron transfer between the photocatalyst and the biofilm as well.

3.4. Proposed removal mechanisms of CIP in the ICPB system

The intermediate products generated in the ICPB system were explored by UPLC-MS. Combined with literature reports and mass spectrometry information on intermediate products (Fig. S10 and Table S2), we speculated about the probable removal pathways of CIP in ICPB system (Fig. 5). The key groups in CIP such as formamide, hydroxyl, keto, dimethylamino and other products can be oxidized to form intermediate products with low toxicity in separate PC process (Zhang et al., 2015). As observed from Table S3, products with M/Z=348, 316, 288 and 291 do not disappear with increased reaction time, and no small molecule intermediates are detected in the PC. This means that the active species produced by PC alone cannot further mineralize these products (Fig. 5, PC accumulated intermediates).

Some small molecule intermediates with M/Z of 245, 263, 274, 156 and 154 are detected in the ICPB (Fig. 5, ICPB produced intermediates) after coupled B, and the appearance of these products shows that organisms can use photocatalytic intermediates in the ICPB and further mineralize these products into small molecule products through metabolic activity (Xie et al., 2018). The bio-photocatalytic system supports the long-term performances of ICPB in treating CIP removal and mineralization.

To predict the toxicity of CIP and its degradation intermediates to aquatic organisms in the PC and ICPB degradation, the acute and chronic toxicities were computed at three nutrient levels. In the Fig. 6 and Table S4, the acute toxicity to fish and daphnia is estimated to be LC_{50}, that to green algae is EC_{50}, and the acute toxicity

of CIP are 13131.42, 1240.43 and 1621.63 mg/L, respectively. The chronic toxicity (ChVs) of CIP to fish, daphnia and green algae are 1553.59, 81.27 and 455.22 mg/L, respectively. According to Chinese hazard evaluation guidelines for new chemical substances (HJ/T 154-2004) and European Union criteria, CIP is harmless to aquatic organisms (Miklos et al., 2018).

For the chronic and acute toxicities of products, except H and K, most intermediates are harmless to three aquatic organisms. The LC_{50}s of fish and ChVs of green algae of all intermediates are greater than 100.0 and 10.0 mg/L in the four degradation pathways, respectively, indicating that these products have no acute toxicity to fish and no chronic toxicity to green algae. In degradation pathway 1, there are no chronic and acute toxicity at three trophic levels. However, a complex trend is observed in the toxic evolutions of degrading intermediates in pathways 2, 3 and 4. H and K are harmful to both fish and green algae and toxic to daphnia. In general, the dangerous products will be generated in the ICPB degradation process using the boron-doped bismuth oxychloride nanosheet catalysts. However, these intermediates can be further detoxified by decomposition of active species and microbes into CO_2 and H_2O after sufficient reaction time, indicating that the ICPB system is very effective for CIP detoxification (Nie et al., 2022).

The survival of microorganisms on the carrier was shown by CLSM (Fig. 7a). From the overall distribution of active bacteria and dead bacteria, the ICPB system can protect the microorganisms inside the carrier to a greater extent compared with the B system. It can be observed that active bacteria decreased in the ICPB and B

degradation, indicating that the microbes on the carrier at the beginning of the reaction have been harmed to a certain extent due to the action of CIP and superoxide radicals and hydroxyl radicals in the ICPB reaction. However, the difference between the ICPB reaction and the B process is that active bacteria and dead bacteria do not change much in the ICPB reaction during the whole reaction, which shows that the toxicity and complexity of CIP are reduced through the PC process. Meanwhile, the microbes inside carrier are protected due to the mesh structure of the carrier, so that there are still a mass of active bacteria in the system at the end of reaction. In addition, the proportion of active bacteria decreased significantly, and the proportion of dead bacteria increased obviously during the B reaction. This is because the degradation effect of microbes on CIP is very small, and with the deepening of the toxic effect of CIP on bacteria, the biofilm on the carrier falls off. These results agree with the literature (Man et al., 2005; Li et al., 2011).

The microbial community analysis shows that the bacterial communities are adjusted after a longer removal procedure. Fig. 7b and Fig. S11 clearly present the microbial community analysis at the genus level. Prior to the reaction (initial), the dominant genera are composed of *Zoogloea*, *Acinetobacter*, *Acidororax* and *Lactobacillus*, which are common genera in the sewage treatment processes (Zhang et al., 2011; Liu et al., 2010). While a new genus emerges in ICPB, *Pseudoxanthomonas*, which is reported to be inherently resistant to CIP (Mohammadi et al., 2013; Olivares et al., 2008; Walsh et al., 2013). Meanwhile, the relative abundance of *Ferruginibacter*, *Clostridium*, *Stenotrophomonas* and *Comamonas* are also gradually

increasing, and some *Clostridium* and *Stenotrophomonas* have the ability to cut aromatic rings as the reaction progresses (Wojcieszynska et al., 2011). There are numerous literature reports that *Ferruginibacter* and *Comamonas* possess the ability of aromatic compounds and their derivatives degradation (Huang et al., 2016). The changes of microbial community richness and diversity in ICPB are shown in Table S5. After ICPB reaction, the Chao 1 and ACE indices of biofilm increased by 23% and 20%, respectively. The Simpson indices decreased while the Shannon indices increased. The increase of Chao 1, ACE and Shannon indices and the decrease of Simpson indices show that the biofilms adapt to CIP, active species and other adverse environmental factors through the succession of its own community structure in ICPB, resulting in the increase of microbial community richness and diversity. In addition, abundant *Lysinibacillus*, *Pseudomonas*, *Burkholderia*, and *Bacillus* have the ability to transfer extracellular electrons, exhibiting the potential of photoelectrons transfer between the microorganisms and photocatalysts (Nandy et al., 2013; Huang et al., 2011). The energy generated by the light-excited photoelectrons can be utilized by microorganisms to rebuild their microbial communities to adapt to the environment. The succession of biological community structure is a manifestation of adaptation to the CIP environment, which is of great significance to the survival of biofilms.

The change of Dehydrogenase Activity (DHA) is also a manifestation of biological self-regulation and adaptation to ICPB system. Dehydrogenase is the key enzyme that converts glucose into pyruvate in glycolysis pathway, which is often used to characterize the activity of microorganisms. Fig. 7c shows the DHA of biofilm on the

carrier in ICPB system. In the first 15 days of ICPB reaction, the DHA of biofilm decreased by 31.17%, which is mainly due to the double damage of microorganisms by high concentration antibiotics and oxidative free radicals in the initial stage of the reaction, and do not adapt to the environment of ICPB reaction. Moreover, the area of photocatalysts exposed on the outside surface of the carrier is small, and the amounts of intermediate products produced by photocatalytic oxidation are less, which leads to the shortage of microbial carbon source. When the carbon source in the environment is insufficient, organisms produce less dehydrogenase to participate in glycolysis process, resulting in a temporary decline in biological activity (Ma et al., 2015).

The initial stage is also the time for microorganisms to adapt to the environment. With the falling off of the biofilm on the carrier surface, a large number of catalysts are exposed, which cannot only reduce the CIP concentration in the solution, but also provide more carbon sources for microbial growth. Therefore, by the 40th day, the DHA of biofilm basically recovered to the unreacted level. This also shows that microorganisms begin to gradually adapt to the environment of photocatalysis-biodegradation synchronous reaction in the middle stage of ICPB reaction. At the same time, the presence of microorganisms prompts PC to oxidize CIP into small molecular substances with relatively simple structure and low toxicity. The microorganisms in the biofilm begin to play a role and the biological activity increased. The recovery of DHA also just proves the existence of biological effects in the process of direct coupling reaction.

4. Conclusions

In this work, the novel ICPB system significantly improves the degradation and mineralization efficiency of CIP using visible light. A degradation rate of ~95% is reached after 40 days demonstrates the ICPB system has excellent degradation stability. Furthermore, the participation of organisms makes the mineralization rate of CIP increase by 20%. Interior biofilms evolve to being enriched in *Pseudoxanthomonas*, *Ferruginibacter*, *Clostridium*, *Stenotrophomonas* and *Comamonas* and regulating their microbial communities using the energy source produced by photoelectrons. Moreover, the diversity and abundance of microbes are enhanced, realizing multifold CIP removal pathways. The advantages of ICPB lie in the complementarity of photocatalysis and biodegradation. Therefore, ICPB enhances degradation and mineralization of CIP, and the lack of cytotoxic effects of its effluents.

CRediT authorship contribution statement

Yilin Dong: Investigation, Writing - Original Draft and Formal analysis. **Dongyu Xu:** Writing - Review & Editing. **Jie Zhang:** Validation. **Qiuwen Wang:** Investigation. **Shaoxuan Pang:** Conceptualization. **Guangming Zhang:** Supervision. **Luiza C Campos:** Validation and Funding acquisition. **Longyi Lv:** Investigation. **Xiaoyang Liu:** Data curation. **Wenfang Gao:** Investigation. **Li Sun:** Validation. **Zhijun Ren:** Supervision and Funding acquisition. **Pengfei Wang:** Supervision, Funding acquisition and Writing - Review & Editing.

Declaration of Competing Interest

The authors declare that they have no known competing financial interests or personal relationships that could have appeared to influence the work reported in this paper.

Acknowledgements

The authors gratefully acknowledge the financially support by the National Natural Science Foundation of China as general projects (grant No. 51779068, 52070066, 52211530084 and 22006029), Science and Technology Research Projects of Colleges and Universities in Hebei province (grant No. ZD2020149), Tianjin Commission of Science and Technology as key technologies R&D projects (21YFSNSN00250), and Royal Society/International Exchanges 2021 Cost Share/NSFC (grant No. IEC\NSFC\211142).

References

Bing, L., Tong, Z., 2010. Biodegradation and adsorption of antibiotics in the activated sludge process. Environ. Sci. Technol. 44 (9), 3468-3473.

Ding, R., Yan, W., Wu, Y., Xiao, Y., Gang, H., Wang, S., Chen, L., Zhao, F., 2018. Light-excited photoelectrons coupled with bio-photocatalysis enhanced the degradation efficiency of oxytetracycline. Water Res. 143, 589-598.

Dong, Y., Xu, D., Wang, Q., Zhang, G., Zhang, Q., Zhang, Z., Lv, L., Xia, Y., Ren, Z., Wang, P., 2021. Tailoring the electronic structure of ultrathin 2D Bi_3O_4Cl sheets by boron doping for enhanced visible light environmental remediation. Appl. Surf. Sci. 542, 148521.

Fu, S., Zhao, X., Zhou, Z., Li, M., Zhu, L., 2021. Effective removal of odor substances using intimately coupled photocatalysis and biodegradation system prepared with the silane coupling agent (SCA)-enhanced TiO_2 coating method. Water Res. 188, 116569.

Huang, Z., Ni, B., Jiang, C., Wu, Y., He, Y., Parales, R.E., Liu, S., 2016. Direct sensing and signal transduction during bacterial chemotaxis towards aromatic compounds in Comamonas testosteroni. Mol. Microbiol. 101, 224-237.

Huang, L., Regan, J.M., Quan, X., 2011. Electron transfer mechanisms, new applications, and performance of biocathode microbial fuel cells. Bioresour. Technol. 102 (1), 316-323.

Kolpin, D., Furlong, E., Meyer, M., Thurman, E.M., Zaugg, S.D., Barber, L.B., Buxton, H.T., 2002. Pharmaceuticals, hormones, and other organic wastewater contaminants in U.S. streams, 1999-2000: a national reconnaissance. Environ. Sci. Technol. 36, 1202-1211.

Kong, X.X., Jiang, J.L., Qiao, B., Liu, H., Cheng, J.S., Yuan, Y.J., 2019. The biodegradation of cefuroxime, cefotaxime and cefpirome by the synthetic consortium with probiotic Bacillus clausii and investigation of their potential biodegradation pathways. Sci. Total Environ. 651, 271-280.

Leong, S., Li, D., Hapgood, K., Zhang, X., Wang, H., 2016. $Ni(OH)_2$ decorated rutile TiO_2 for efficient removal of tetracycline from wastewater. Appl. Catal. B: Environ. 198, 224-233.

Li, J., Cai, L., Shang, J., Yu, Y., Zhang, L., 2016. Giant enhancement of internal

electric field boosting bulk charge separation for photocatalysis. Adv. Mater. 28, 4059-4064.

Li, J., Pei, Q., Wang, R., Zhou, Yong., Zhang, Z., Cao, Q., Wang, D., Mi, W., Du, Y., 2018. Enhanced photocatalytic performance through magnetic field boosting carrier transport. ACS Nano. 12, 3351-3359.

Li, G., Park, S., Kang, D.W., Krajmalnik-Brown, R., Rittmann, B.E., 2011. 2,4,5-Trichlorophenol degradation using a novel TiO_2-coated biofilm carrier: roles of adsorption, photocatalysis, and biodegradation. Environ. Sci. Technol. 45, 8359-8367.

Li, G., Park, S., Rittmann, B., 2012a. Developing an efficient TiO_2-coated biofilm carrier for intimate coupling of photocatalysis and biodegradation. Water Res. 46 (19), 6489-6496.

Li, G., Park, S., Rittmann, B., 2012b. Degradation of reactive dyes in a photocatalytic circulating-bed biofilm reactor. Biotechnol. Bioeng. 109, 884-893.

Liu, Y., Kong, Y., Zhang, R., Zhang, X., Wong, F., Tay, J., Zhu, J., Jiang, W., Liu, W., 2010. Microbial population dynamics of granular aerobic sequencing batch reactors during start-up and steady state periods. Water Sci. Technol. 62, 1281-1287.

Ma, D., Zou, D., Zhou, D., Li, T., Dong, S., Xu, Z., Dong, S., 2015. Phenol removal and biofilm response in coupling of visible-light-driven photocatalysis and biodegradation: Effect of hydrothermal treatment temperature. Int. Biodeterior. Biodegradation. 104, 178-185.

Man, S.L., Hong, S.S., Mohseni, M., 2005. Synthesis of photocatalytic nanosized TiO_2-Ag particles with sol-gel method using reduction agent. J. Mol. Catal. A-Chem. 242 (1), 135-140.

Marsolek, M.D., Rittmann, B.E., 2015. Effect of substrate characteristics on microbial community structure, function, resistance, and resilience; application to coupled photocatalytic-biological treatment. Water Res. 90, 1-8.

Marsolek, M.D., Torres, C.I., Hausner, M., Rittmann, B.E., 2008. Intimate coupling of photocatalysis and biodegradation in a photocatalytic circulating-bed biofilm reactor. Biotechnol. Bioeng. 101, 83-92.

Miklos, D.B., Remy, C., Jekel, M., Linden, K.G., Drewes, J.E., Hubner, U., 2018. Evaluation of advanced oxidation processes for water and wastewater treatment-a critical review. Water Res. 139, 118-131.

Mirzaei, A., Chen, Z., Haghighat, F., Yerushalmi, L., 2017. Removal of pharmaceuticals from water by homo/heterogonous Fenton-type processes-a review. Chemosphere. 174, 665-688.

Mohammadi, N.S., Mafakheri, S., Abdali, N., Tauch, A., Benz, R., 2013. Identification and characterization of the channel-forming protein in the cell wall of Corynebacterium amycolatum. Biochim Biophys Acta. 1828, 2574-2582.

Nandy, A., Kumar, V., Kundu, P.P., 2013. Utilization of proteinaceous materials for power generation in a mediatorless microbial fuel cell by a new electrogenic bacteria Lysinibacillus sphaericus VA5. Enzym. Microb. Technol. 53 (5), 339-344.

Nie, X., Li, G., Li, S., Luo, Y., Luo, W., Wan, Q., An, T., 2022. Highly efficient

adsorption and catalytic degradation of ciprofloxacin by a novel heterogeneous Fenton catalyst of hexapod-like pyrite nanosheets mineral clusters. Appl. Catal. B: Environ. 300, 120734.

Olivares, J., Bernardini, A., Garcialeon, G., Corona, F., Sanchez, M.B., Martinez, J.L., 2013. The neglected intrinsic resistome of bacterial pathogens. PLoS One. 4 (2), e1619.

Park, J., Nam, H., Choi, J., Ha, J., Lee, S., 2017. Oxidation of geosmin and 2-methylisoborneol by the photo-Fenton process: kinetics, degradation intermediates, and the removal of microcystin-LR and trihalomethane from Nak-Dong River water, South Korea. Chem. Eng. J. 313, 345-354.

Qiao, M., Ying, G.G., Singer, A.C., Zhu, Y.G., 2018. Review of antibiotic resistance in China and its environment. Environ Int. 110, 160-172.

Shi, H., Yu, Y., Zhang, Y., Feng, X., Zhao, X., Tan, H., Khan, S.U., Li, Y., Wang, E., 2018. Polyoxometalate/TiO_2/Ag composite nanofibers with enhanced photocatalytic performance under visible light. Appl. Catal. B: Environ. 221, 280-289.

Walsh, F., Duffy, B., 2013. The culturable soil antibiotic resistome: a community of multi-drug resistant bacteria. PLoS One. 8 (6), e65567.

Wang, D., Bolton, J.R., Andrews, S.A., Hofmann, R., 2015. Formation of disinfection by-products in the ultraviolet/chlorine advanced oxidation process. Sci. Total Environ. 518, 49-57.

Wen, D., Li, G., Xing, R., Park, S., Rittmann, B.E., 2012. 2, 4-DNT removal in

intimately coupled photobiocatalysis: the roles of adsorption, photolysis, photocatalysis, and biotransformation. Appl. Microbiol. Biotechnol. 95 (1), 263-272.

Wojcieszynska, D., Guzik, U., Gren, I., Perkosz, M., 2011. Hupert-Kocurek K, Induction of aromatic ring: cleavage dioxygenases in Stenotrophomonas maltophilia strain KB2 in cometabolic systems. World J. Microbiol. Biotechnol. 27, 805-811.

Xie, Z., Feng, Y., Wang, F., Chen, D., Zhang, Q., Zeng, Y., Lv, W., Liu, G., 2018. Construction of carbon dots modified MoO_3/g-C_3N_4 Z-scheme photocatalyst with enhanced visiblelight photocatalytic activity for the degradation of tetracycline. Appl. Catal. B: Environ. 229, 96-104.

Xiong, H., Zou, D., Zhou, D., Dong, S., Wang, J., Rittmann, B.E., 2017. Enhancing degradation and mineralization of tetracycline using intimately coupled photocatalysis and biodegradation (ICPB). Chem. Eng. J. 316, 7-14.

Yu, F., Li, Y., Han, S., Ma, J., 2016. Adsorptive removal of antibiotics from aqueous solution using carbon materials. Chemosphere. 153, 365-385.

Zhang, B., Ji, M., Qiu, Z., Liu, H., Li, J., 2011. Microbial population dynamics during sludge granulation in an anaerobic-aerobic biological phosphorus removal system. Bioresource Technol. 102, 2474-2480.

Zhang, L., Xing, Z., Zhang, H., Li, Z., Wu, X., Zhang, X., Zhang, Yan., Zhou, Wei., 2016. High thermostable ordered mesoporous SiO_2-TiO_2 coated circulating-bed biofilm reactor for unpredictable photocatalytic and biocatalytic performance.

Appl. Catal. B: Environ. 180, 521-529.

Zhang, X., Li, R., Jia, M., Wang, S., Huang, Y., Chen, C., 2015. Degradation of ciprofloxacin in aqueous bismuth oxybromide (BiOBr) suspensions under visible light irradiation: a direct hole oxidation pathway. Chem. Eng. J. 274, 290-297.

Zhang, Y., Hong, L., Shi, W., Pu, X., Zhang, H., Rittmann, B.E., 2010. Photobiodegradation of phenol with ultraviolet irradiation of new ceramic biofilm carriers. Biodegradation. 21 (6), 881-887.

Zhang, Y., Wang, B., Cagnetta, G., Duan, L., Yang, J., Deng, S., Huang, J., Wang, Y., Yu, G., 2018. Typical pharmaceuticals in major WWTPs in Beijing, China: occurrence, load pattern and calculation reliability. Water Res. 140, 291-300.

Zhou, D., Dong, S., Shi, J., Cui, X., Ki, D., Torres, C.I., Rittmann, B.E., 2017. Intimate coupling of an N-doped TiO_2 photocatalyst and anode respiring bacteria for enhancing 4-chlorophenol degradation and current generation. Chem. Eng. J. 317, 882-889.

Zhou, D., Xu, Z., Dong, S., Huo, M., Dong, S., Tian, X., Cui, B., Xiong, H., Li, T., Ma, D., 2015. Intimate coupling of photocatalysis and biodegradation for degrading phenol using different light types: visible light vs UV light. Environ. Sci. Technol. 49, 7776-7783.

Figure captions

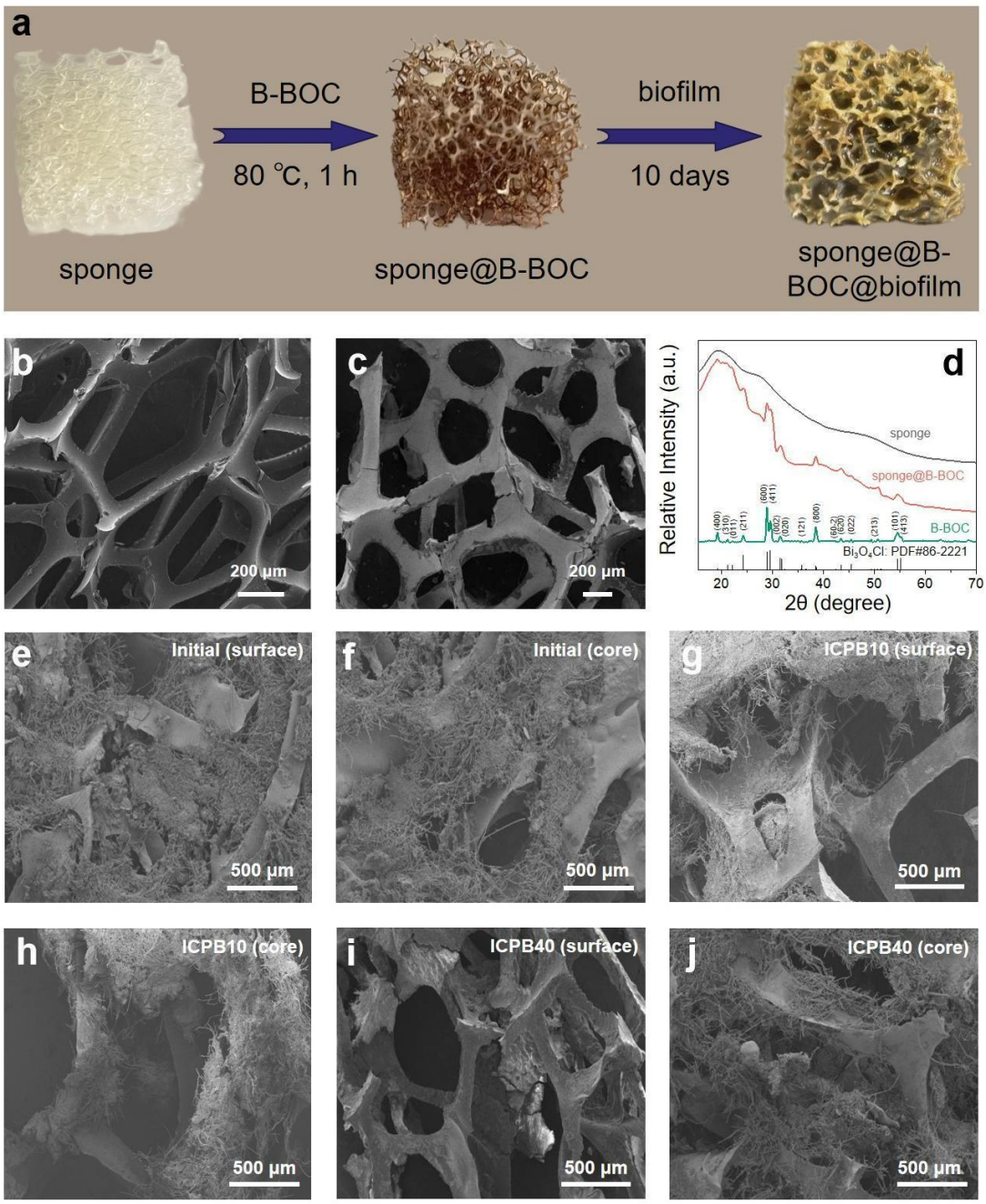

Fig. 1. (a) Schematic diagram of the synthetic routes of sponge@B-BOC@biofilm. SEM images of (b) sponge, (c) sponge@B-BOC, (d) XRD patterns of blank sponge, B-BOC and sponge@B-BOC. SEM images of (e) surface and (f) core of sponge@B-BOC@biofilm, after sponge@B-BOC@biofilm operation for (g, h) 10 days and (i, j) 40 days in the ICPB system.

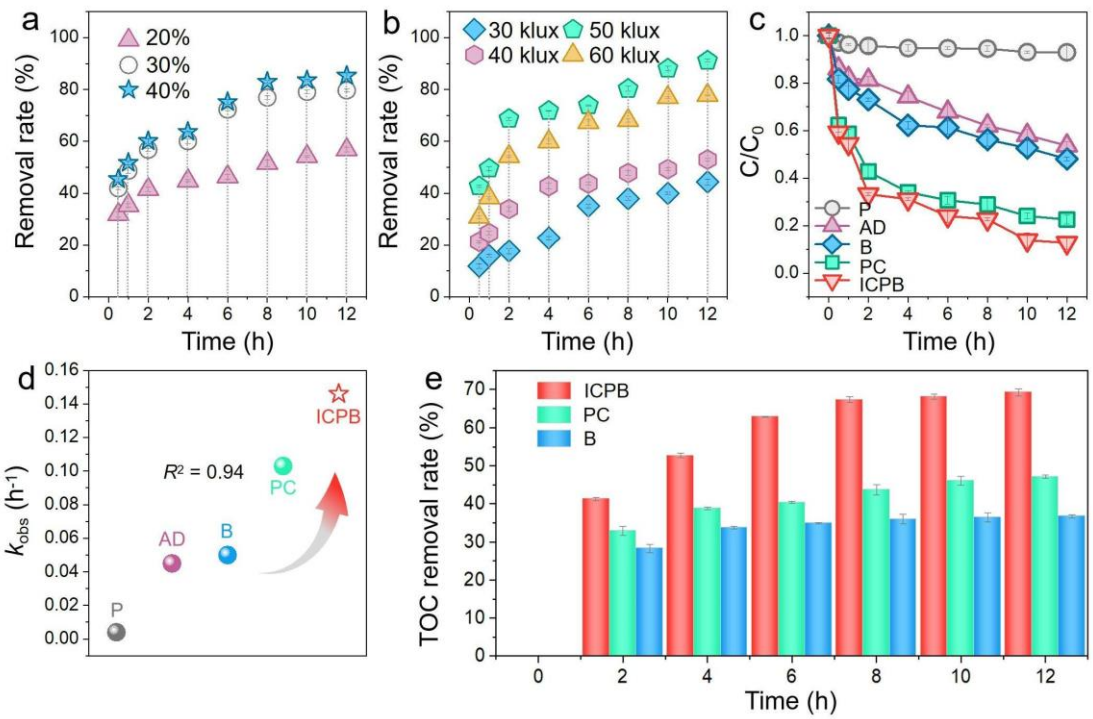

Fig. 2. (a) The CIP degradation of ICPB system at different (a) carrier dosage and (b) light intensity. (c) Removal of CIP and (d) first-order rate constants of CIP removal in P, AD, B, PC, and ICPB systems. (e) The TOC removal rate after B, PC, and ICPB operation after 12 h.

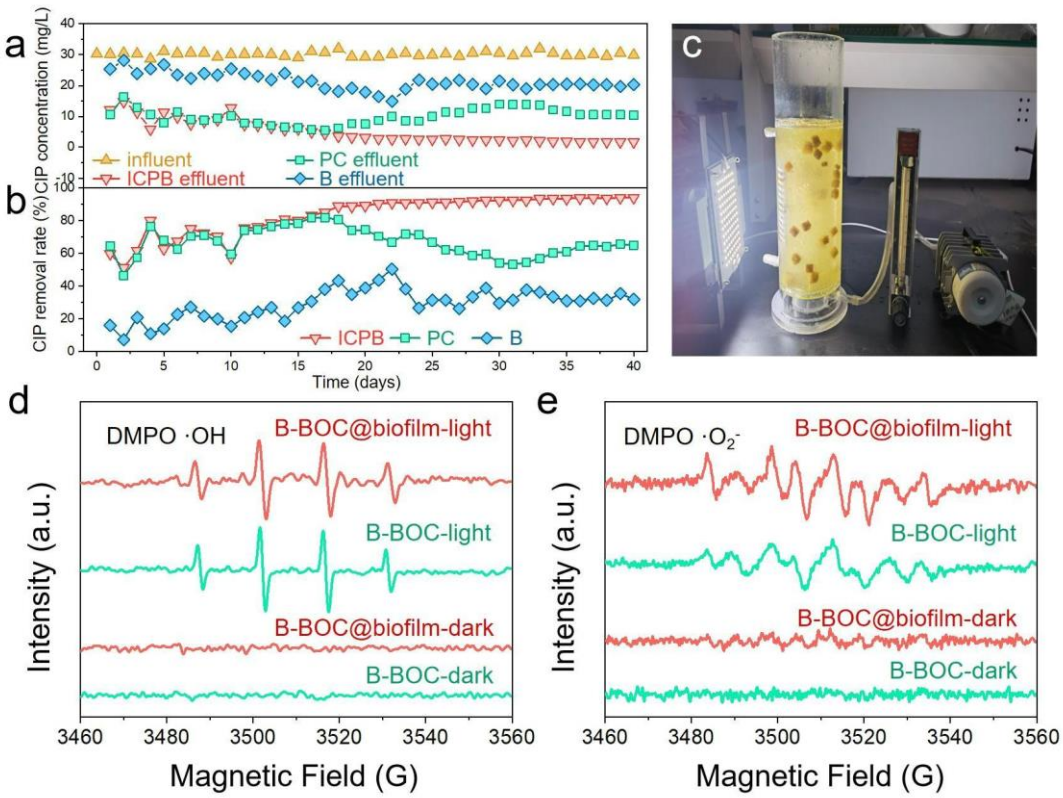

Fig. 3. (a), (b) B, PC and ICPB degradation in the perturbation system. (c) The photo of CIP (totally 30 mg/L) degradation device. ESR spectra of B-BOC and B-BOC@biofilm in the existence of (d) DMPO-·OH and (e) DMPO-·O_2^-, respectively.

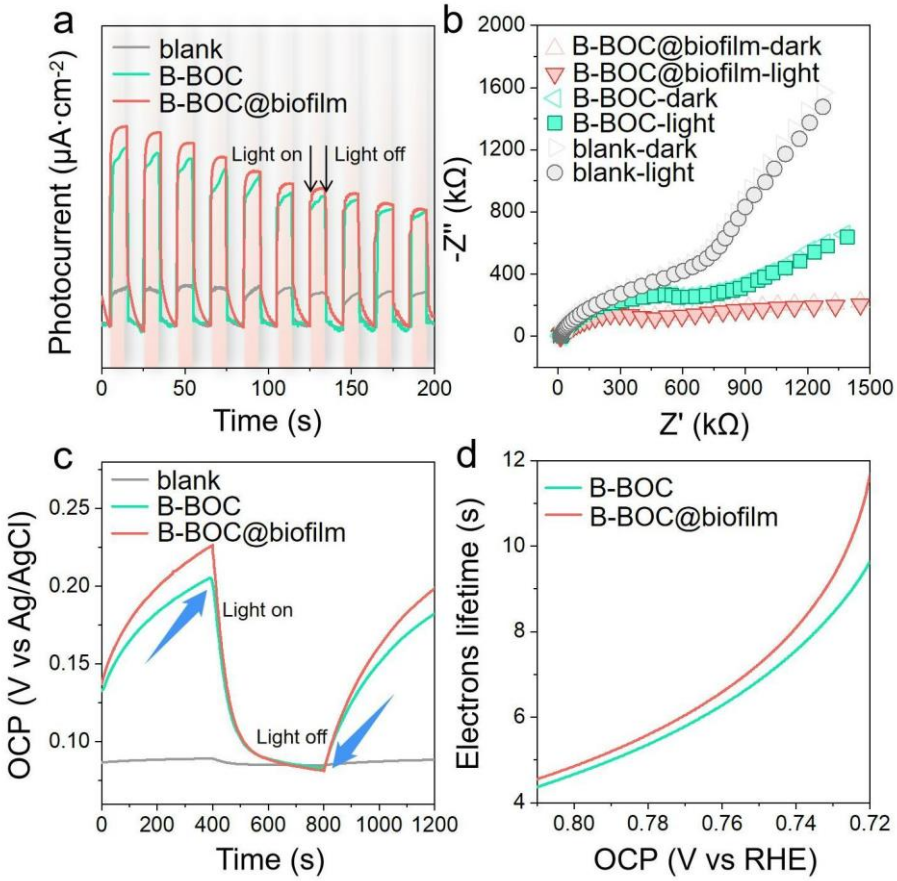

Fig. 4. (a) Photocurrent responses, (b) photo-electrochemical impedance spectroscopy and (c) time dependence of open circuit potential of PC and ICPB system. (d) Electron lifetime as a function of open-circuit potential.

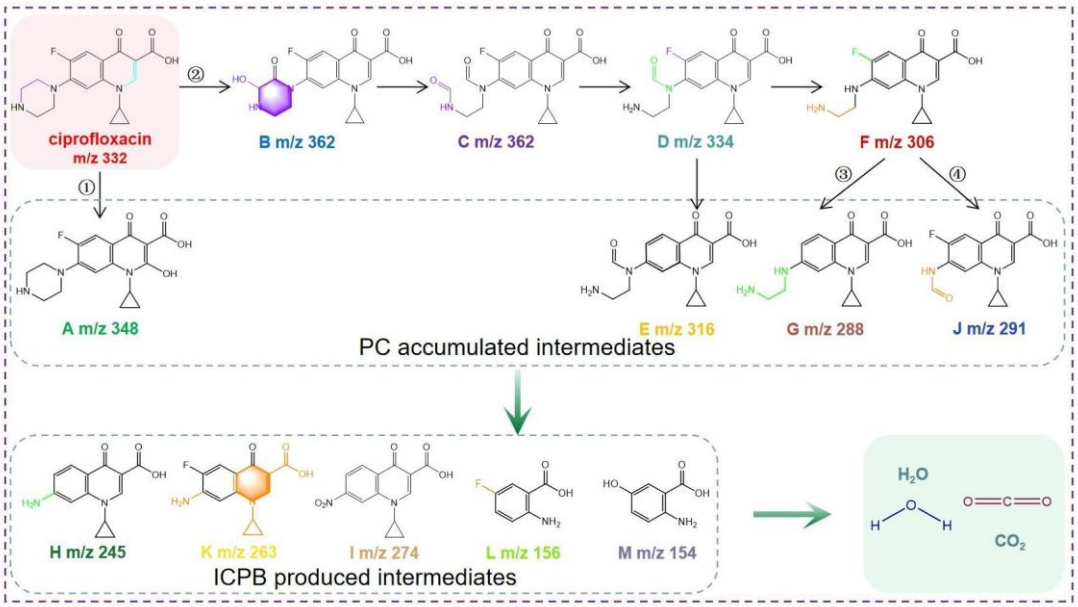

Fig. 5. The possible transformation pathways of CIP degradation.

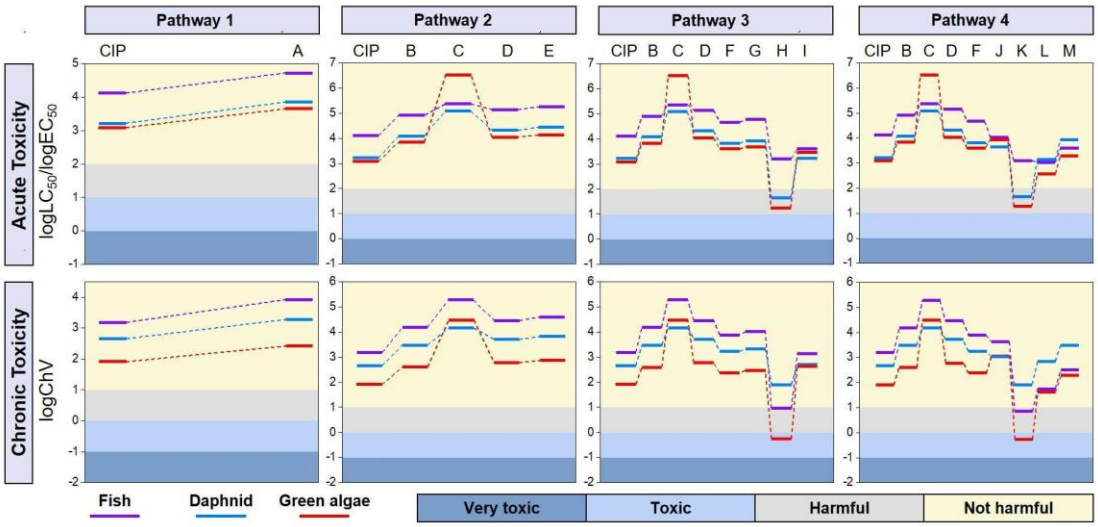

Fig. 6. Acute and chronic toxicity evolution of CIP and its degradation intermediates toward three aquatic organisms using EPI Suite software with ECOSAR program.

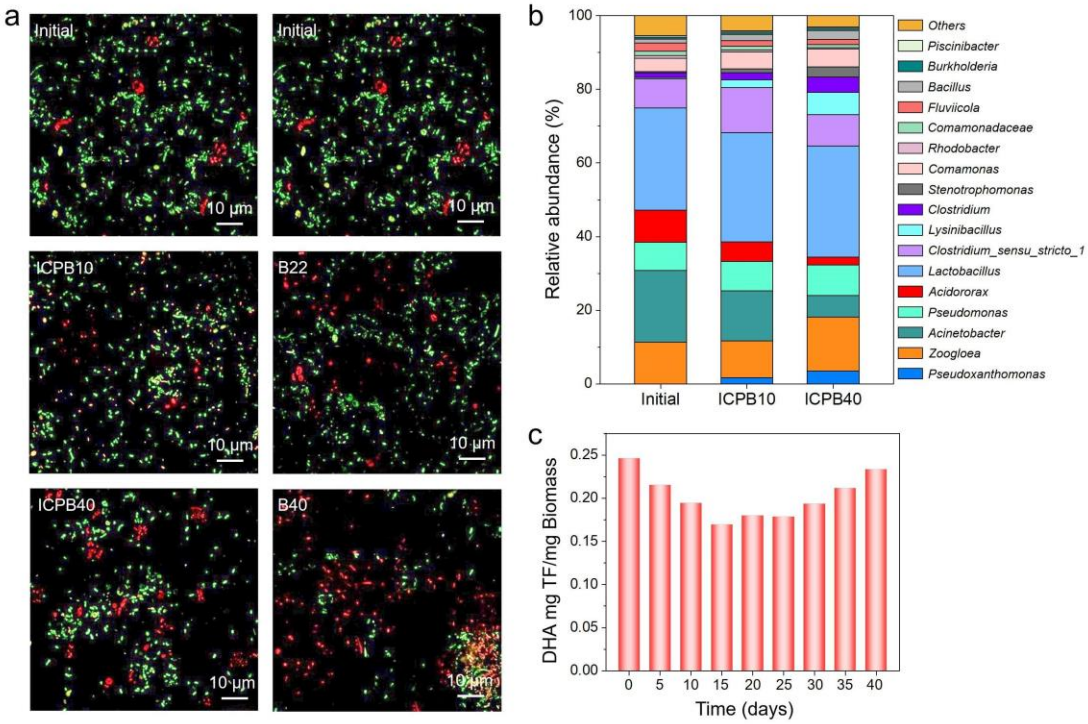

Fig. 7. (a) The CLSM images of CIP degradation during ICPB and B systems. (b) Relative abundances of the biofilm genera before (Initial) and after (ICPB) the degradation experiment. (c) Variation of microbial dehydrogenase activity during CIP degradation by ICPB.

Supplementary materials

Enhanced antibiotic wastewater degradation by intimately coupled B-Bi_3O_4Cl photocatalysis and biodegradation reactor: Elucidating degradation principle systematically

Yilin Dong [a,b], Dongyu Xu [a,b], Jie Zhang [a,b], Qiuwen Wang [a,b], Shaoxuan Pang [a,b], Guangming Zhang [a,b], Luiza C Campos [c], Longyi Lv [a,b], Xiaoyang Liu [a,b], Wenfang Gao [a,b], Li Sun [a,b], Zhijun Ren [a,b,*], Pengfei Wang [a,b,*]

a School of Energy and Environmental Engineering, Hebei University of Technology, Tianjin 300401, China

b Tianjin Key Laboratory of Clean Energy and Pollutant Control, Tianjin 300401, China

c Department of Civil, Environmental and Geomatic Engineering, University College London, London WC1E 6BT, United Kingdom

*Correspondence to: Z. J. Ren (E-mail: renzhijun2003@126.com) & P. F. Wang (E-mail: pengfeiwang@hebut.edu.cn)

Text S1. Preparation of B-BOC photocatalyst

0.243 g of $Bi(NO_3)_3 \cdot 5H_2O$, 0.2 g polyvinyl pyrrolidone (PVP, K30) and 0.3 mL H_3BO_3 solution (20 g/L) were diffused into 15 mL mannitol solution (0.1 mol/L) to acquire solution A. Totally, the solution B was obtained by 0.5 mmol NaCl dissolved into 3 mL mannitol solution (0.1 mol/L). Then, solution B and solution A by magnetic stirring for 30 min, adjust the pH to 11.5 with NaOH solution (2 M). After that, the suspension was sealed in a 50 mL Teflon-lined stainless-steel autoclave, and then the autoclave was kept at 160 °C for 24 h in oven. After cooled down to normal temperature, the solid substances were gathered by centrifugation and washed with deionized water and anhydrous ethanol for three times, respectively, then dried under vacuum at 60 °C all night.

Text S2. Experimental set-up.

CIP degradation was conducted in an internal loop airlift-driven fluidized bed reactor with a working volume of 800 mL (Fig. S4). The reaction device is made of plexiglass, which is mainly composed of two inner and outer hollow cylinders. The height of the outer hollow cylinder is 220 mm, and the outer diameter and inner diameter are 100 mm and 90 mm, respectively. The height of the inner concentric annular column is 170 mm, the outer diameter and inner diameter are 60 mm and 50 mm, respectively, and four 20 mm×20 mm rectangular channels are set at the bottom. The inner annular cylinder is nested in the annular space between the outer annular cylinder and the bottom aeration disc. The bottom of the reactor is provided with an aeration disc with the same diameter as the inner wall sleeve.

Text S3. Characteristic of B-BOC

The morphology of B-BOC was observed by using an SU8000 scanning electron microscope (SEM, Hitachi, Japan) at an accelerating voltage of 3-5 kV and a Tecnai G20 (FEI Co., Holland) microscope operated at an accelerating voltage of 200 kV. The transmission electron microscopy (TEM) images were tested using Tecnai G2 and FEI Co to acquire morphology of the photocatalysts. Powder X-ray diffractometry (XRD) was obtained by a Bruker D8 diffractometer with Cu Kα radiation. The specific surface area tests were performed with an ASAP 2020 system using the Brunauer-Emmett-Teller (BET) method. The pore size distributions were estimated by the Barret-Joyner-Halenda (BJH) method. X-ray photoelectron spectroscopy (XPS) was collected by a 5300 ESCALAB spectrometer to explore the surface chemical element. UV-Vis absorption spectra of the photocatalysts were proceeded using a UV-vis spectrophotometer (U-3900H, Shimadzu).

Text S4. Pretreatment for SEM observation

Biofilms attached to carriers were prepared for SEM by washing them with 0.01 M phosphate buffered saline (PBS) and fixing them with 2.5% (wt) glutaraldehyde for 30 min, and then frozen at -20 °C. We visualized interior of the carriers by slicing the carriers with a sterile razor blade prior to gold coating and then observed with an SEM instrument (JSM-7500F; Japan).

Text S5. Staining and confocal laser scanning microscopy (CLSM) imaging

The carrier samples attached with biofilm were washed with PBS for three times, fixed with 4 wt% paraformaldehyde at 4 °C for 4 h, and then washed with PBS again. Then the pretreated samples were frozen and sliced. Followed by staining using staining activity assay kit (L-7012, LIVE/DEAD® BacLight TM, USA). The sections were then placed on microscope slides and analyzed using a CLSM instrument (LEICA TCS SP5, Germany).

Text S6. Measurement of Dehydrogenase Activity (DHA)

First, 20 sponge carriers were removed from the reactor and placed in a 50 mL centrifuge tube. Add 2.5 mL distilled water, 5 mL TTC solution (4 mg/mL), 2 mL glucose solution (0.1 mol/L) and 2 mL Tris-HCl buffer solution (7.874 g/L, pH = 8.4) successively. Put the centrifuge tube into an oscillator (200 rpm) and shake for 20 min. Then put it into a constant temperature incubator (37 ℃) for 1 h, and drop concentrated sulfuric acid to terminate the reaction. Finally, triphenylmethane (TC) in the solution was extracted with 5 mL toluene, and the centrifuge tube was placed in an oscillator to vibrate (200 rpm) for 30 min before ultrasonic treatment 8 min. The mixed solution is centrifuged at the speed of 4000 rpm for 5 min after standing for 3 min. The supernatant is taken to measure its absorbance at 485 nm. The dehydrogenase activity of the sample can be obtained by comparing with the standard curve.

Table S1. First-order loss rates of CIP (k) based on First-order kinetic simulation in PC and ICPB protocols.

	k/h^{-1}	R^2
ICPB	0.15	0.94
PC	0.10	0.91

Table S2. Identification of the possible CIP degradation products by LC-MS under visible light irradiation.

Compounds	Formula	m/z	Proposed structure
CIP	$C_{17}H_{18}FN_3O_3$	332	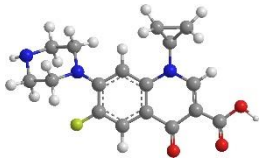
A	$C_{17}H_{18}FN_3O_4$	348	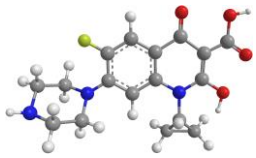
B	$C_{17}H_{16}FN_3O_5$	362	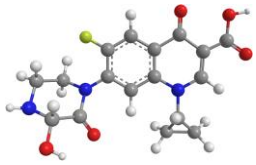
C	$C_{17}H_{16}FN_3O_5$	362	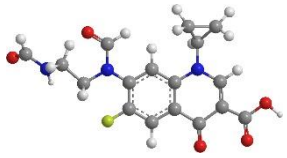
D	$C_{16}H_{16}FN_3O_4$	334	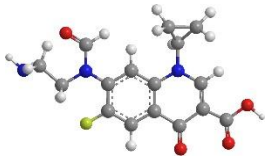
E	$C_{16}H_{17}N_3O_4$	316	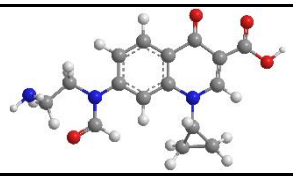
F	$C_{15}H_{16}FN_3O_3$	306	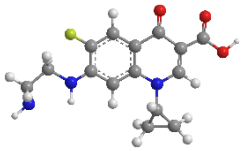
G	$C_{15}H_{17}N_3O_3$	288	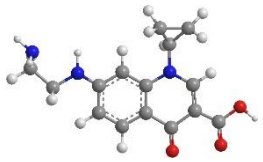

H	$C_{13}H_{13}N_2O_3$	245	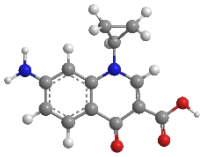
I	$C_{13}H_{10}N_2O_5$	274	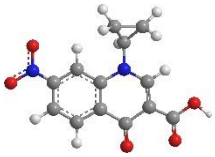
J	$C_{14}H_{11}FN_2O_4$	291	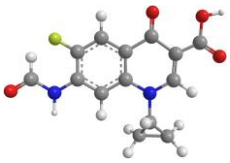
K	$C_{13}H_{11}FN_2O_3$	263	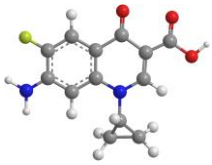
L	$C_7H_6FNO_2$	156	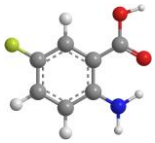
M	$C_7H_7NO_3$	154	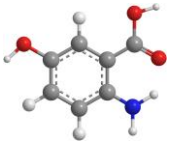

Table S3. Sampling time of and detected intermediate products (▲:detected intermediate products).

Sampling time (h)		Intermediate products (M/Z)												
		332	362	334	306	348	316	291	288	245	274	263	156	154
Initial		▲												
2	PC	▲	▲	▲	▲	▲	▲	▲	▲					
	ICPB	▲		▲						▲				
4	PC	▲		▲		▲	▲	▲	▲					
	ICPB	▲		▲	▲					▲				▲
6	PC	▲				▲	▲	▲						
	ICPB	▲			▲					▲	▲			▲
8	PC	▲				▲	▲							
	ICPB	▲	▲		▲					▲	▲	▲		▲
10	PC	▲					▲							
	ICPB	▲	▲							▲	▲	▲		▲
12	PC	▲												
	ICPB	▲	▲							▲	▲	▲	▲	▲

Table S4. Theoretical calculated data of aquatic toxicity of CIP and its degradation intermediates.

		Acute toxicity LC/EC$_{50}$ (mg·L^{-1})			Chronic toxicity ChV (mg·L^{-1})		
	m/z	Fish	Daphnid	Green Algae	Fish	Daphnid	Green Algae
CIP	332	13131.42	1240.43	1621.63	1553.59	81.27	455.22
A	348	52549.06	4478.23	7177.09	8508.76	265.45	1870.63
B	362	84487.11	6963.03	11923.15	15149.01	399.53	3033.57
C	362	2.37×10^5	3.30×10^5	$1,21\times10^5$	1.94×10^5	30476.44	14351.49
D	334	1.41×10^5	11096.86	20792.34	29027.43	609.16	5119.36
E	316	1.81×10^5	13888.21	27250.19	39922.38	745.31	6597.62
F	306	47270.91	4021.27	6467.45	7695.74	237.96	1683.51
G	288	60239.46	5006.45	8431.79	10528.80	289.62	2158.28
H	245	1648.64	17.84	47.28	9.15	0.57	78.41
I	274	4212.61	3014.28	1696.70	1392.18	438.47	494.84
J	291	10323.43	8571.98	4387.36	4179.46	1126.60	1045.67
K	263	1283.55	19.07	45.48	7.06	0.54	76.91
L	156	1053.02	372.42	1384.45	56.71	42.58	663.67
M	154	4005.65	1932.88	8458.99	324.58	202.28	3101.89

Very toxic	Toxic	Harmful	Not harmful

Table S5. Richness and diversity indices obtained by high throughput sequencing.

Samples	Chao1 indexes	ACE indexes	Simpson indexes	Shannon indexes
Initial	1329	1583	0.073	4.30
ICPB40	1631	1892	0.054	6.74

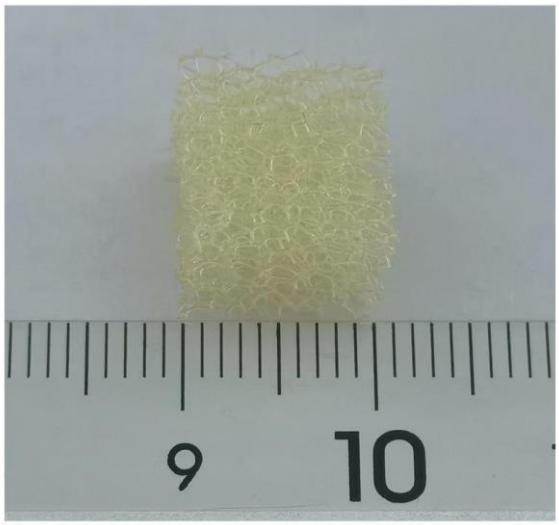

Fig. S1. Picture of polyurethane sponge carriers.

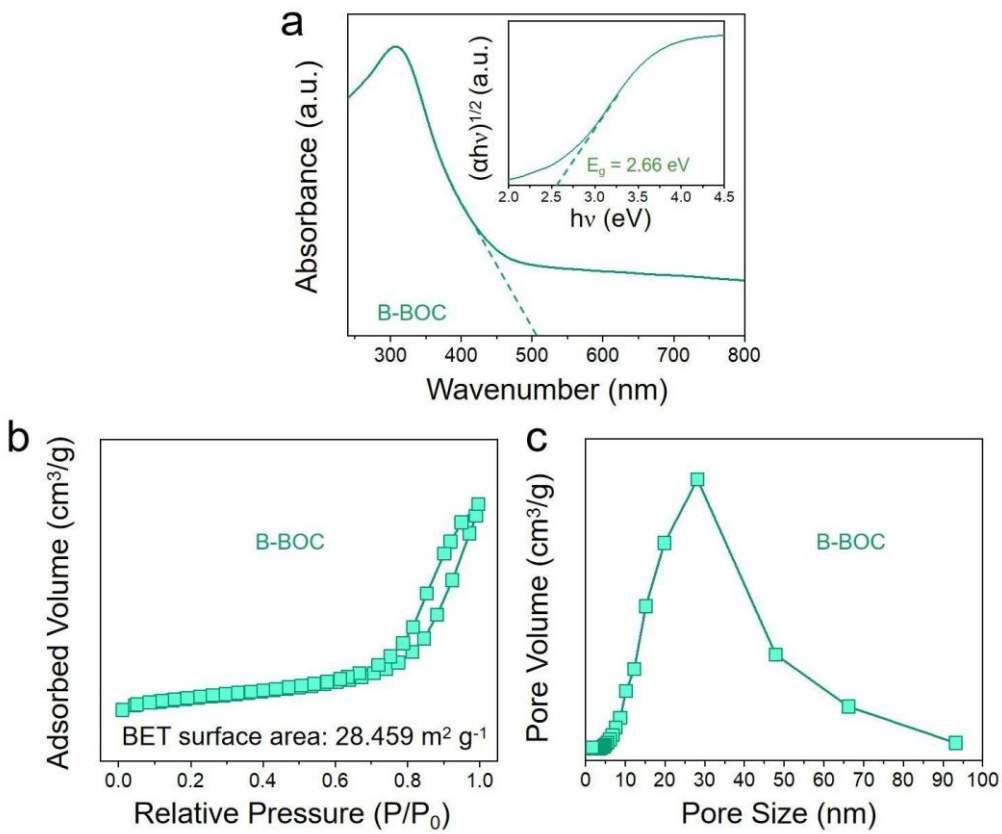

Fig. S2. (a) Ultraviolet-visible diffuse reflectance spectra of B-BOC with the inset showing the band gap energy (E_g) of B-BOC. (b) N_2 adsorption/desorption isotherm curve and (c) BJH pore size distribution of B-BOC.

The absorption property and energy band characteristics of as-prepared B-BOC photocatalyst were analyzed by UV-vis diffuse reflectance spectra (DRS) as displayed in Fig. S2a. A broad light absorption centered at 503 nm was observed for B-BOC in the visible light range, which implies that B-BOC is easy to produce photogenerated charge carriers, thus enhancing its photocatalytic efficiency. The curves of conversion $(ah\nu)^{n/2}$ versus hν were plotted by absorption spectrum, and the band gap energies (E_g) were calculated by using the formula: $ah\nu = A(h\nu - E_g)^{n/2}$, in which a, h, ν, A and E_g represent the absorption coefficient, Planck constant, light frequency, proportionality constant and the band gap, respectively (Che et al., 2018). Note that the optical

transitions type of a semiconductor decides the value of n. As previously reported, the value of n for BOC is 1 (Xu et al., 2014). As shown in Fig. S2a (inset), evidently, B-BOC has an energy gap of 2.66 eV, resulting B-BOC has a wide absorption of visible light.

In order to evaluate the effect of specific surface areas on degradation performance, the pore size distribution and specific surface areas of the prepared sample were analyzed by BJH and BET methods. As shown in Fig. S2b, the isotherm of the material showed Type IV curve with a hysteresis loop at a high relative pressure between 0.6 and 1.0 (Huang et al., 2014). The shape of the hysteresis loop is close to Type H3, indicating the sample is a meso-porous structure (Liu et al., 2018). This result is further supported by the pore size distribution (Fig. S2c). The specific surface area of B-BOC is 28.459 m^2g^{-1}.

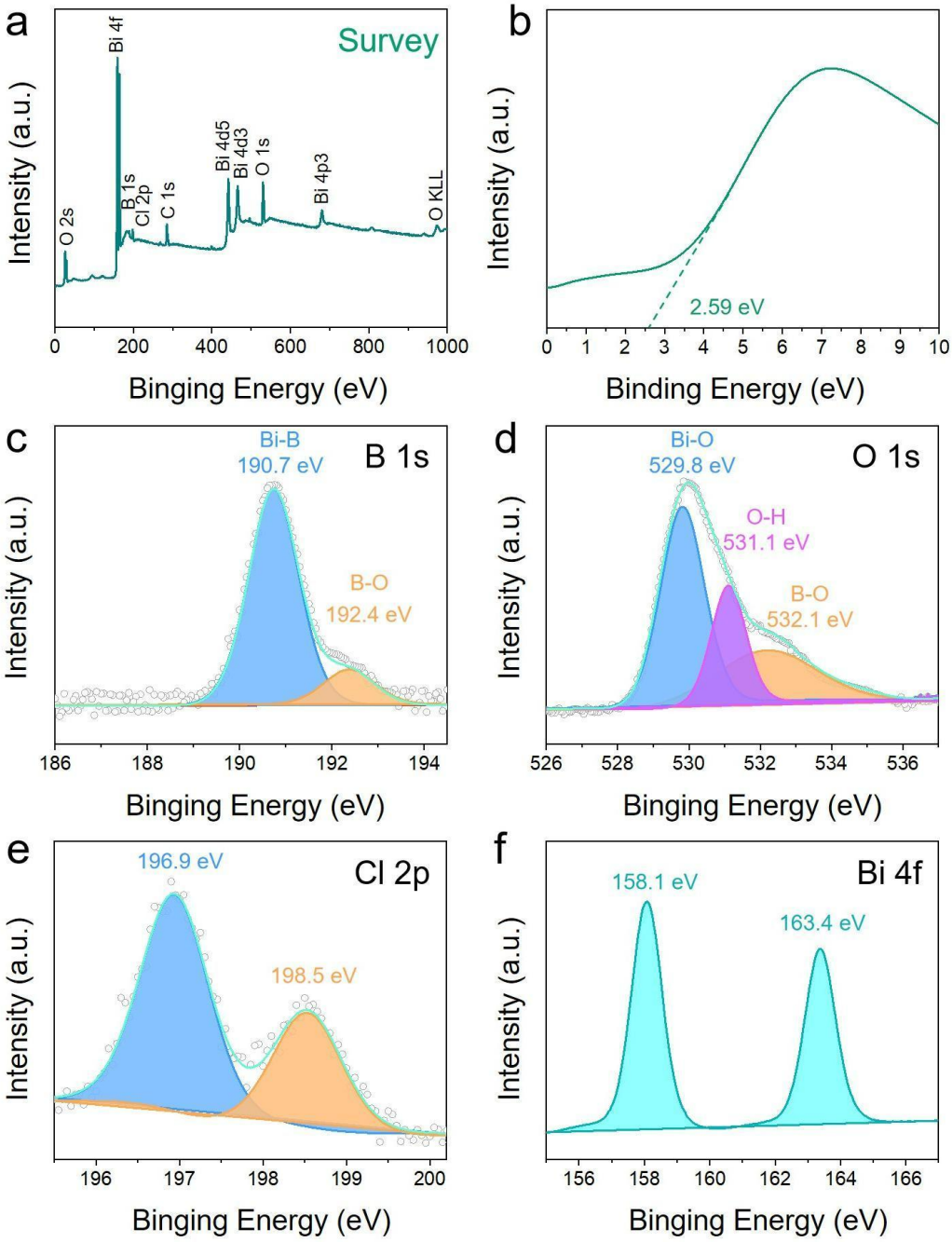

Fig. S3. (a) XPS survey spectra, (b) valence-band (VB) XPS spectra, (c) B 1s XPS spectra, (d) O 1s XPS spectra, (e) Cl 2p XPS spectra, (f) Bi 4f XPS spectra of the B-BOC.

It is worth noting that the XPS survey spectra showed that all the elements of Bi, O, Cl and B were present in the B-BOC photocatalyst (Fig. S3a). In addition, the VB of photocatalyst was determined by XPS valence spectra (Fig. S3b). And the VB

maximum of B-BOC is assessed to be 2.59 eV, which can be used to calculate the band structure of the sample in subsequent studies. The doping state of B was analyzed by X-ray photoelectron spectroscopy (XPS) (Fig. S3c-f). As shown in Fig. S3c, the B 1s peaks are observed at binding energy of 190.7 eV and 192.4 eV for B-BOC, which belong to the Bi-B bonds and B-O bonds, respectively (Yu et al., 2019). Furthermore, the peaks of O 1s were located at 529.8 eV, 531.1 eV and 532.2 eV, corresponding to Bi-O bonds, O-H bonds and B-O bonds, respectively (Fig. S3d) (Yang et al., 2016). Then, in the high-resolution Cl 2p spectra of B-BOC (Fig. S3e), the Cl 2p peaks of 198.5 eV and 196.9 eV correspond to the $2p_{3/2}$ and $2p_{1/2}$ orbitals of Cl^-, respectively. At the same time, Bi 4f XPS spectra showed two peaks at 163.4 eV and 158.1 eV, which were equivalent to the Bi $4f_{5/2}$ and Bi $4f_{7/2}$, and distributed to Bi^{3+} in the sample (Fig. S3f).

Fig. S4. Schematic diagram of the photocatalytic circulating-bed biofilm reactor.

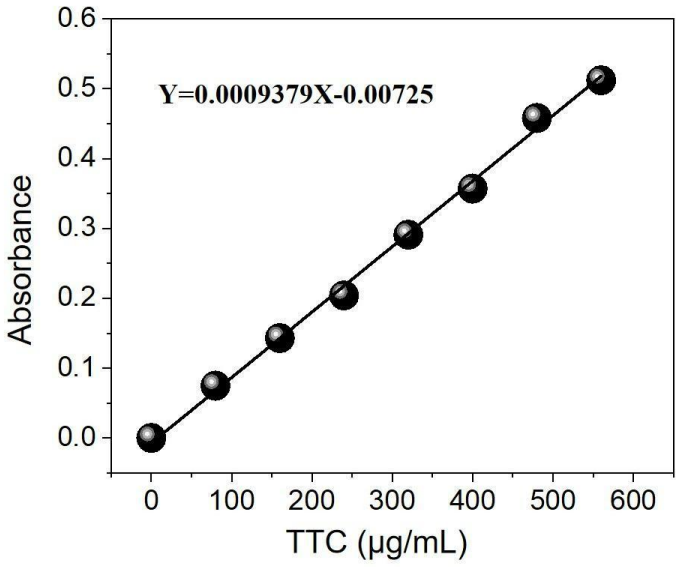

Fig. S5. TTC-DHA standard curve.

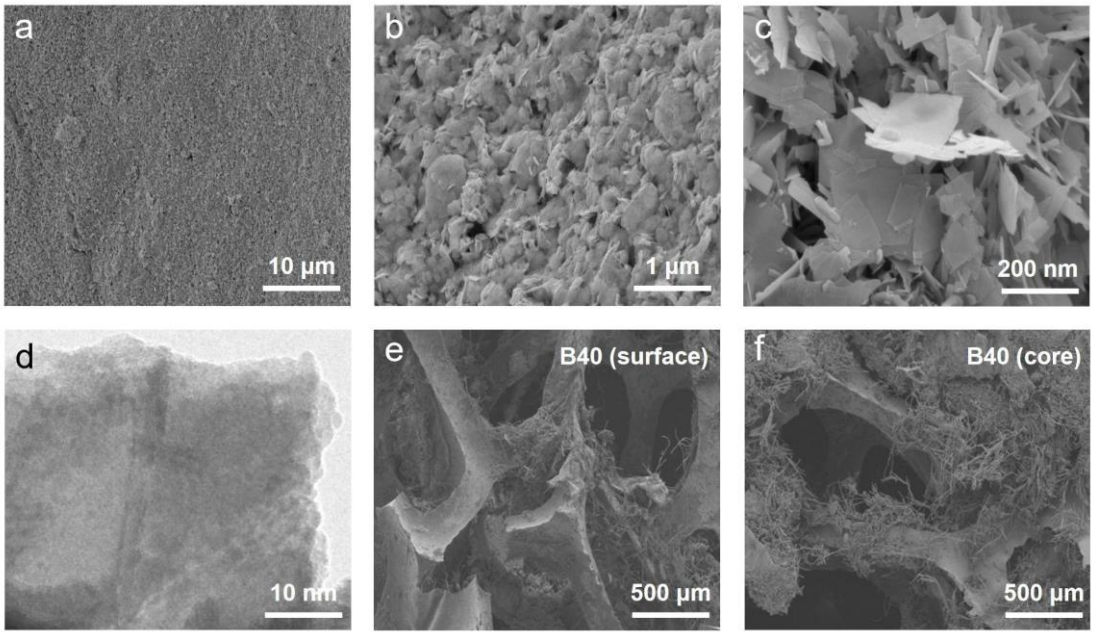

Fig. S6. (a, b, c) SEM images of sponge@B-BOC. (d) TEM images of B-BOC nanosheets. SEM images of (e) surface and (f) core of after sponge@B-BOC@biofilm operation for 40 days in the B system.

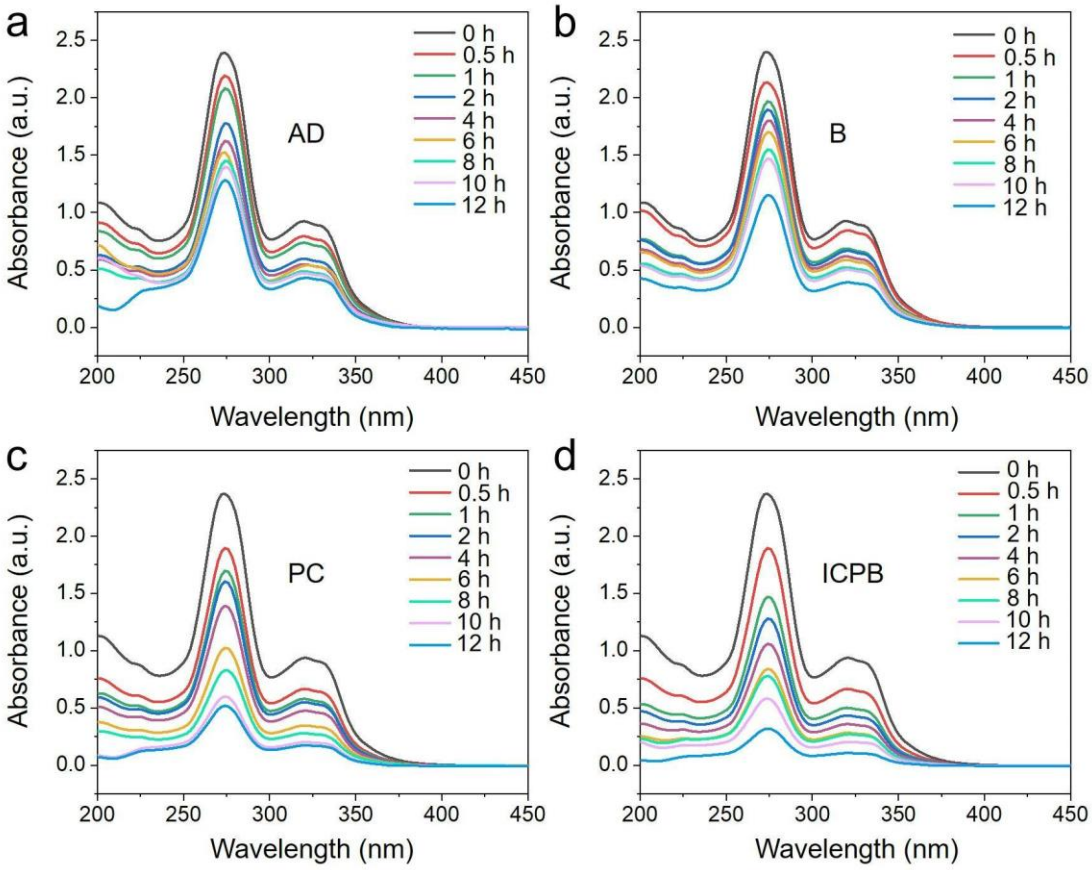

Fig. S7. Changes of UV-vis spectrums of CIP solutions in (a) AD, (b) B, (c) PC and (d) ICPB along the operating time of 12 h.

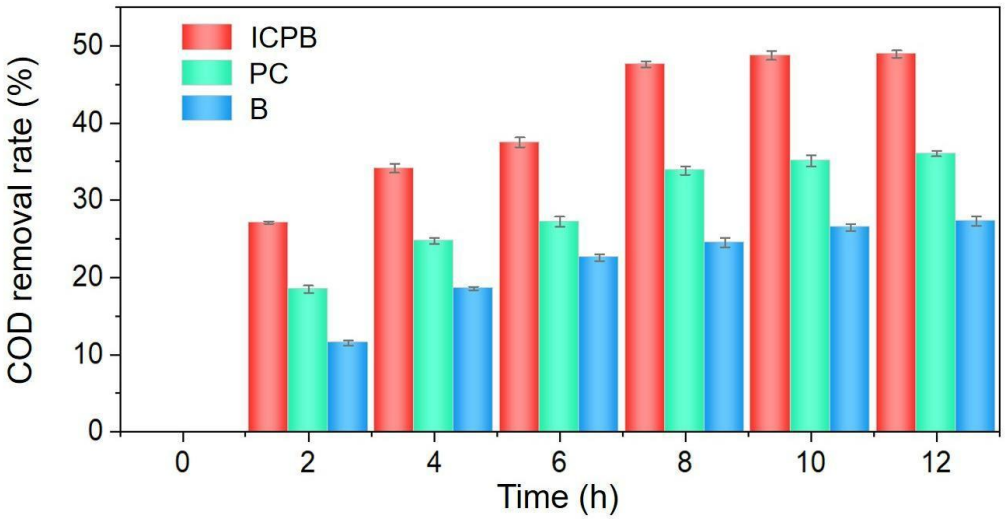

Fig. S8. The COD removal rate after B, PC, and ICPB operation after 12 h.

As can be seen from Fig. S8, the removal rate of COD is 27.3% in the separate biodegradation (B), indicating that CIP is difficult to biodegradate, which is basically consistent with the degradation efficiency of CIP in B. The removal efficiency of CIP by photocatalytic oxidation is about 80%, while the removal rate of COD is much lower than that of CIP, which indicates that photocatalysis has a poor effect on CIP mineralization. Many researchers have found that CIP is difficult to be completely mineralized by advanced oxidation. In comparison, the biological participation makes the removal rate of COD by ICPB significantly improved. Among the intermediates produced by photocatalysis in ICPB, the biodegradable intermediates are directly utilized by organisms, which not only maintains the activity of biofilm, but also improves the degradation and mineralization efficiency of CIP.

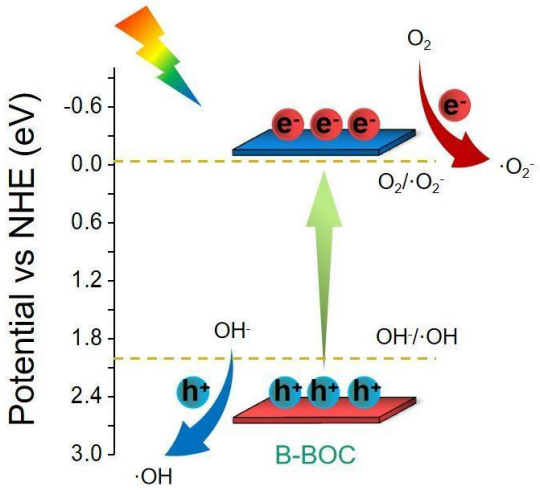

Fig. S9. Schematic energy level diagram of B-BOC.

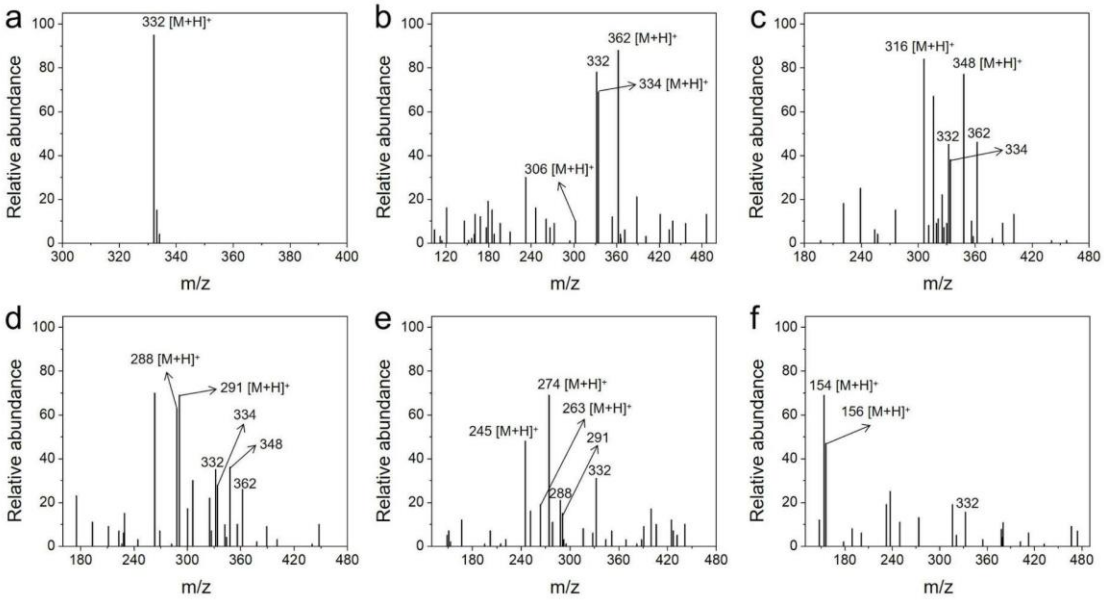

Fig. S10. M/z of CIP and intermediates eluted at different time. The parent ions correspond to the pseudo molecular peak ions $[M+H]^+$.

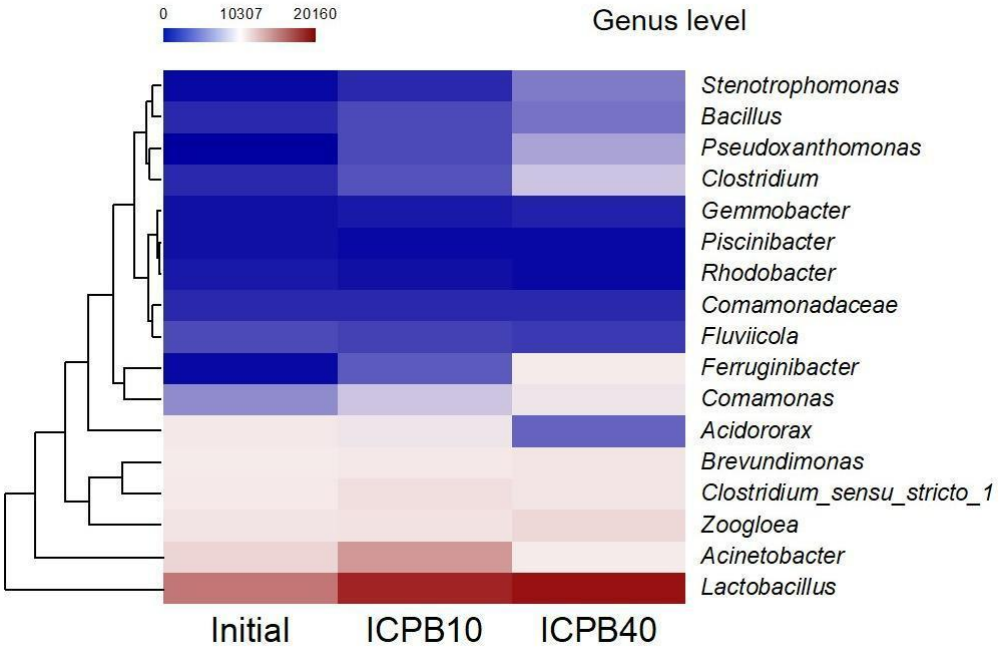

Fig. S11. Pyrosequencing results of DNA from the microbial community before (Initial) and after (ICPB) the ICPB degradation at the genus levels.

References

Che, H.N., Liu, C.B., Hu, W., Hu, H., Li, J.Q., Dou, J.Y., Shi, W.D., Li, C.M., Dong, H.J., 2018. NGQD active sites as effective collectors of charge carriers for improving the photocatalytic performance of Z-scheme g-C_3N_4/Bi_2WO_6 heterojunctions. Catal. Sci. Technol. 8, 622-631.

Huang, S.T., Jiang, Y.R., Chou, S.Y., Dai, Y.M., Chen, C.C., 2014. Synthesis, characterization, photocatalytic activity of visible-light-responsive photocatalysts BiO_xCl_y/BiO_mBr_n by controlled hydrothermal method. J. Mol. Catal. A: Chem. 391, 105-120.

Liu, F.Y., Jiang, Y.R., Chen, C.C., Lee, W.W., 2018. Novel synthesis of $PbBiO_2Cl$/BiOCl nanocomposite with enhanced visible-driven-light photocatalytic activity. Catal. Today. 300, 112-123.

Xu, L., Bu, F.X., Hu, M., Jin, C.Y., Jiang, D.M., Zhao, Z.J., Zhang, Q.H., Jiang, J.S., 2014. Monocrystalline mesoporous metal oxide with perovskite structure: a facile solid-state transformation of a coordination polymer. Chem. Commun. 50, 13849-13852.

Yang, W., Zhang, L., Xie, J., Zhang, X., Liu, Q., Yao, T., Wei, S., Zhang, Q., Xie, Y., 2016. Enhanced photoexcited carrier separation in oxygen-doped $ZnIn_2S_4$ nanosheets for hydrogen evolution. Angew. Chem. Int. Ed. 55, 6716-6720.

Yu, C., He, H., Fan, Q., Xie, W., Liu, Z., Ji, H., 2019. Novel B-doped BiOCl nanosheets with exposed (001) facets and photocatalytic mechanism of enhanced degradation efficiency for organic pollutants. Sci. Total. Environ. 694, 133727.